Editors' Suggestion

Temperature-induced structural and electronic phase transitions in λ-phase Ti_3O_5

K. Yoshimatsu [1,2,*] H. Nakao [3] and H. Kumigashira [1,2]

[1]*Institute of Multidisciplinary Research for Advanced Materials, Tohoku University, Sendai, Miyagi 980-8577, Japan*
[2]*Materials Research Center for Element Strategy (MCES), Tokyo Institute of Technology, Yokohama 226-8503, Japan*
[3]*Institute of Materials Structure Science, High Energy Accelerator Research Organization, Oho, Tsukuba 305-0801, Japan*

(Received 19 September 2023; accepted 26 February 2024; published 13 March 2024)

We investigated changes in the structural and electronic properties of single-crystalline Ti_3O_5 films across temperature-induced phase transitions. Based on resistivity and synchrotron x-ray diffraction measurements, we determined the phase diagram of Ti_3O_5. The characteristic properties of Ti_3O_5 were classified into three temperature regions: the insulating λ phase at $T \leqslant 350$ K, the conductive λ phase at 350 K $\leqslant T \leqslant 460$ K via the metal-insulator transition, and the metallic α phase at $T \geqslant 460$ K. Detailed crystallographic analysis revealed that the monoclinic λ phase exhibited a second-order structural phase transition to the orthorhombic α phase, accompanied by a gradual deformation of the monoclinic angle. These results suggest that unusual temperature-induced changes in Ti_3O_5 originate from similar atomic conformations of the λ and α phases. Our findings provide guidelines for controlling multiple phase transitions in Ti_3O_5 polymorphs using external stimuli, which is crucial for optoelectronic and heat-storage applications of Ti_3O_5.

DOI: 10.1103/PhysRevMaterials.8.035002

I. INTRODUCTION

Polymorphs are of great interest in materials chemistry and engineering because of their distinct physical properties originating from their individual atomic conformations [1–8]. Controlling polymorphs is crucial for designing functional materials. For example, in widegap semiconductors such as SiC and Ga_2O_3, the band gap and carrier mobility that govern the performance of electronic devices differ among polymorphs [2,3,6]. In titanium dioxide (TiO_2), photocatalytic performance is controllable among the rutile, anatase, and brookite polymorphs by changing valence and conduction band positions [8].

Trititanium pentoxide (Ti_3O_5), which is an identical titanate class to TiO_2, has five polymorphs of α, β, γ, δ, and λ phases [1,9–14]. Among these phases, metastable λ-phase Ti_3O_5 (λ-Ti_3O_5) with a monoclinic crystal structure ($C2/m$, $a = 9.838$ Å, $b = 3.787$ Å, $c = 9.971$ Å, $\beta = 91.26°$ [11]), which can be stabilized in nanosized forms, has attracted considerable attention for applications and fundamental research because it undergoes phase transition to other polymorphs by external stimuli, such as light, pressure, and temperature [11–24]. Persistent and reversible photoinduced phase transition between the λ and β phases with a monoclinic structure ($C2/m$, $a = 9.752$ Å, $b = 3.802$ Å, $c = 9.442$ Å, $\beta = 91.55°$ [10]) was induced by irradiating nanosecond visible pulse lasers at room temperature, which is unique to Ti_3O_5 among other oxides. Ti_3O_5 polymorphs are thus candidate materials for application in rewritable optical recording media [7,9]. In addition, hydrostatic pressure induced another persistent phase transition from the λ to the β phase [17]. Also, λ-Ti_3O_5 can store the heat of 12 kJ mol^{-1} through the transition and release it by applying tens of MPa pressure, thereby also making it a candidate material for heat-storage application [17,18,24].

For temperature stimulus, the λ phase transformed into the α phase with an orthorhombic crystal structure (*Cmcm*, $a = 3.798$ Å, $b = 9.846$ Å, $c = 9.988$ Å) at ∼450 K [12]. The temperature-induced phase transition contrasts with the photo- and pressure-induced ones, wherein the λ phase transforms into the monoclinic β phase. Therefore, experimental and theoretical studies have been conducted to reveal the origin of the temperature-induced phase transition [12,22,25–28]. However, electrical and structural behaviors across the temperature-induced phase transition are still unclear because no electronic properties across the structural phase transition have been investigated yet due to difficulty in measuring electrical properties of λ-Ti_3O_5 nanoparticles. Moreover, structural information is limited in measuring polycrystalline nanoparticles, which leaves a fundamental issue of how the λ phase transforms into the α phase along the crystallographic directions.

In this paper, we investigated the temperature-induced phase transition in λ Ti_3O_5 using the advantages of a single-crystalline film. Sizable single-crystalline λ-Ti_3O_5 films, which we recently succeeded in synthesizing [29], enable us to investigate the structural and electrical properties in detail. Based on resistivity and synchrotron x-ray diffraction measurements, we constructed a phase diagram of λ-Ti_3O_5, which was classified into three temperature regions. The electronic ground state of the λ phase was an insulator. A conductive λ phase appeared at 350 K $\leqslant T \leqslant$ 460 K across a metal-insulator transition (MIT) at 350 K. With increasing temperature, the monoclinic λ phase showed the second-order structural phase transition to the orthorhombic α phase, characterized by gradual deformation of the monoclinic angle. Eventually, the metallic α phase was stabilized >460 K. These

*yoshimatsu.k.aa@m.titech.ac.jp

results suggest that unusual temperature-induced structural and electronic phase transitions of Ti_3O_5 originate from similar atomic conformations of the λ and α phases.

II. EXPERIMENTS

Here, λ-Ti_3O_5 films were grown on $LaAlO_3$ (110) substrates using the pulsed-laser deposition method. TiO_2 single-crystal substrates (3N purity, Shinkosha Co. Ltd.) were used as a PLD target. A KrF excimer laser (1.1 J/cm^2, 5 Hz) was used for target ablation. The substrate temperature was set at 1100 °C. Ar gas (6N purity) was continuously fed into a PLD chamber to set the chamber pressure to 1×10^{-4} Torr. After film deposition, samples were immediately quenched while maintaining the chamber pressure, which prevented film oxidation during cooling [30,31]. Details of the thin film growth are described elsewhere [29]. The film thickness was ∼100 nm, as measured using cross-sectional transmission electron microscopy (TEM) and a stylus-type profiler. The in-plane and out-of-plane epitaxial relationships were λ-Ti_3O_5 [010]//$LaAlO_3$ [001] and λ-Ti_3O_5 [100]//$LaAlO_3$ [110], respectively, which was determined in our previous report [29].

Synchrotron XRD measurements were performed from 300 to 520 K at BL4C of Photon Factory, KEK. Here, λ-Ti_3O_5 films were heated in a vacuum to prevent oxidation during the measurements. The photon energy was set at 8 keV (λ = 1.5498 Å). Symmetric λ-Ti_3O_5 600 and asymmetric λ-Ti_3O_5 60 ± 1 reflections were recorded to determine the lattice parameters of the films. A coplanar geometry, in which a fixed χ angle (=0°) and individual ω angles are set, was applied to record the λ-Ti_3O_5 601 and 60–1 reflections.

Temperature-dependent resistivity (ρ-T) measurements were carried out on λ-Ti_3O_5 films using a standard four-probe method in a heating procedure up to 650 K. Here, Au (50 nm)/Ti (50 nm) electrodes were deposited on the films by a sputtering method to form Ohmic contact at the film/electrode interface.

III. RESULTS

Figure 1(a) shows the ρ-T curve of the λ-Ti_3O_5 film. Thanks to the large area and single-crystal nature of the film, a reliable ρ-T curve of λ-Ti_3O_5 was obtained. As shown in Fig. 1(a), the ρ-T curve exhibited complicated behaviors. The film showed an insulating behavior ($d\rho/dT < 0$) at low temperatures. With increasing temperature, a resistivity kink was observed at 350 K, suggesting the occurrence of a MIT. As the temperature further increased, the resistivity gradually decreased, and eventually, metallic conductivity ($d\rho/dT > 0$) appeared above ∼590 K [inset of Fig. 1(a)].

To assess the complicated resistivity behaviors, we fitted the ρ-T curve based on the Mott variable-range hopping (VRH) model, which describes well the electrical conduction governed by hopping of localized carriers in a strongly disordered system [33,34]. Adopting this model is most appropriate for λ-Ti_3O_5 film/$LaAlO_3$ substrate specimens since localized carriers may originate from possible charge/orbital order, as discussed later, and the strong disorder might be caused by defects in the films due to completely different crystal structures of the film and substrate. In the Mott VRH model, ρ in

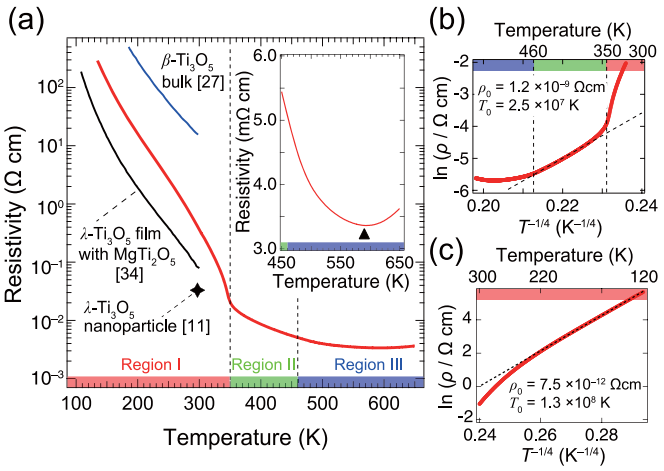

FIG. 1. (a) Temperature-dependent resistivity (ρ-T) of λ-Ti_3O_5 films. The resistivity data of λ-Ti_3O_5 nanoparticles (marker) [11], λ-Ti_3O_5/$MgTi_2O_5$ multilayer (black line) [32], and β-Ti_3O_5 bulk (blue line) [27] are shown for comparison. The inset shows magnification at high temperatures. The filled triangle indicates the data point where $d\rho/dT = 0$. Logarithmic resistivity ln(ρ) vs $T^{-1/4}$ in (b) high-temperature and (c) low-temperature regions. Dashed black lines in (b) and (c) indicate the results of the linear fits based on the Mott variable-range hopping model in three-dimensional conduction.

the three-dimensional system is described as follows:

$$\rho(T) = \rho_0 \exp\left(\frac{T}{T_0}\right)^{-1/4}, \quad (1)$$

where ρ_0 is a pre-exponential term, and T_0 is a characteristic temperature representing the strength of carrier localization [34]. Figures 1(b) and 1(c) show the logarithmic resistivity ln(ρ) as a function of $T^{-1/4}$ in high- and low-temperature regions, respectively. Here, ln(ρ) vs $T^{-1/4}$ was well fitted by a straight line with individual parameters ($\rho_0 = 1.2 \times 10^{-9}$ Ω cm, $T_0 = 2.5 \times 10^7$ K in 350 K ⩽ T ⩽ 460 K and $\rho_0 = 7.5 \times 10^{-12}$ Ω cm, $T_0 = 1.3 \times 10^8$ K in T ⩽ 300 K). For T ⩾ 460 K, ln(ρ) vs $T^{-1/4}$ deviated from the fitted straight line, suggesting another transition. These results suggest that the behaviors of the ρ-T curve are categorized into three characteristic temperature regions. Hereafter, we define the temperature regions T ⩽ 350 K, 350 K ⩽ T ⩽ 460 K, and T ⩾ 460 K as regions I, II, and III, respectively.

To investigate the relationship between the structural and electrical properties, we performed temperature-dependent XRD measurements. Figure 2(a) shows the representative temperature-dependent XRD patterns of the λ-Ti_3O_5 600 reflections. The λ-Ti_3O_5 600 reflections taken in the whole measurement temperature are shown in Fig. 6(a) (see Appendix A). Variations in the peak intensity are seen in Fig. 2(a). The peak intensity remained intact in region I (300–350 K), whereas it drastically decreased in region II (from 350 to 460 K) and then reversibly increased in region III (from 460 to 500 K). The intensity variation was caused by the change in the peak width along the ω direction, as discussed later (Fig. 4). These results suggest a close relationship between the transport properties and structural changes in Ti_3O_5.

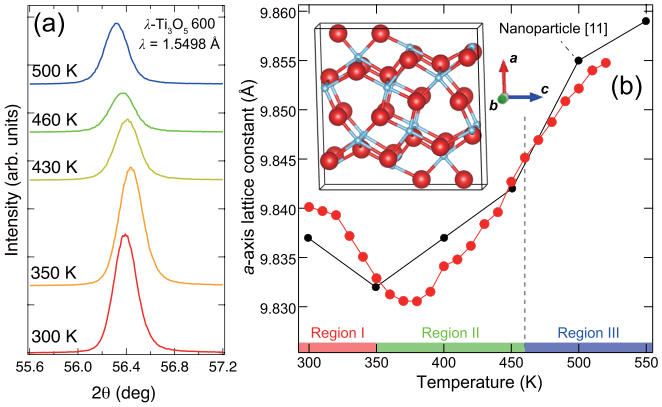

FIG. 2. (a) Representative temperature-dependent synchrotron x-ray diffraction (XRD) patterns of λ-Ti_3O_5 600 reflections. Temperature-dependent XRD patterns taken in the whole temperature are shown in Fig. 6(a), see Appendix A. (b) Temperature-dependent a-axis lattice constants of λ-Ti_3O_5 films. The data of λ-Ti_3O_5 nanoparticles are also plotted for comparison [11]. The inset shows the crystal structure of λ-Ti_3O_5 projected along the a-c plane drawn using VESTA [35].

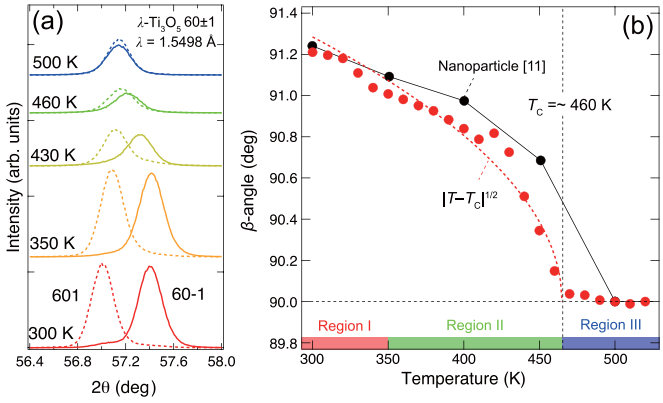

FIG. 3. (a) Representative temperature-dependent synchrotron x-ray diffraction (XRD) patterns of λ-Ti_3O_5 60 ± 1 reflections. Temperature-dependent XRD patterns taken in the whole temperature are shown in Figs. 6(b) and 6(c), see Appendix A. The dashed and solid lines indicate 601 and 60–1 reflections, respectively. (b) Temperature-dependent monoclinic β angle. The data of λ-Ti_3O_5 nanoparticles are also plotted for comparison [11].

Closer inspection reveals that the peak position slightly shifts toward higher 2θ angles in region I, indicating that the a-axis lattice constant became smaller. In contrast, it shifted toward lower 2θ angles in regions II and III, indicating that the a-axis lattice constant became larger. The lattice elongation was consistent with a difference in the lattice constants between the high-temperature α phase ($b = 9.846$ Å) [12] and the low-temperature λ phase ($a = 9.838$ Å) [11].

The temperature-dependent a-axis lattice constants determined from the λ-Ti_3O_5 600 reflections were summarized in Fig. 2(b). Although the overall feature is consistent with the reported results of λ-Ti_3O_5 nanoparticles [11], a much smaller temperature step in this paper reveals detailed temperature-induced structural changes. The a-axis lattice constants were continuous in temperatures, but the sign of a thermal lattice expansion (da/dT) was reversed ∼350 K, which would be attributed to the MIT. The temperature-dependent a-axis lattice deformation in λ-Ti_3O_5 is in sharp contrast to that across the temperature-induced first-order phase transition in β-Ti_3O_5 (from the monoclinic β phase to the orthorhombic α phase), where the a-axis lattice constant was discontinuous at a critical temperature [12].

Next, to investigate the change in the crystalline phase in temperatures, we performed the temperature-dependent XRD measurements around λ-Ti_3O_5 60 ± 1 reflections. Figure 3(a) shows the representative temperature-dependent XRD patterns of the λ-Ti_3O_5 60 ± 1 reflections. The λ-Ti_3O_5 60 ± 1 reflections taken in the whole measurement temperature were shown in Figs. 6(b) and 6(c) (see Appendix A). The λ-Ti_3O_5 601 and 60–1 reflections were detected at each corresponding 2θ angle in region I (300–350 K), reflecting the monoclinic crystal structure. In region II, they got closer with increasing temperature and were almost overlapped at 460 K. Eventually, the λ-Ti_3O_5 60 ± 1 reflections reached an identical 2θ angle at 500 K (region III). These results suggest a structural phase transition from the monoclinic to orthorhombic crystal structures.

To discuss the structural phase transition quantitatively, we determined a monoclinic angle (β angle) using the d values of the λ-Ti_3O_5 60 ± 1 reflections ($d_{60\pm1}$) and a-axis lattice constants. Figure 3(b) shows the plot of the β angle as a function of temperature. The β angle was 91.21° at 300 K, which was consistent with that of λ-Ti_3O_5 nanoparticles ($\beta = 91.26°$) [11]. Although it slightly became smaller even in region I, it drastically dropped toward 90° in region II, and eventually, it saturated to 90° in region III, confirming the transition from the monoclinic to orthorhombic crystal structures. The temperature-dependent β angle of the film was in good agreement with that of λ-Ti_3O_5 nanoparticles [11]; the change in crystal symmetry was attributed to the structural phase transition from monoclinic λ-Ti_3O_5 to orthorhombic α-Ti_3O_5. Thus, it is naturally concluded that the temperature-induced phase transition in λ-Ti_3O_5 films is the second-order one from the monoclinic λ phase to the orthorhombic α phase, as in the case of the nanoparticles. The β angle was an order parameter in the second-order structural phase transition [36,37]. Its temperature dependence followed a relationship of $\propto |T - T_C|^{1/2}$ below the critical temperature (T_C) of ∼460 K, as shown with the dotted line in Fig. 3(b). We thus determined the phase-transition temperature identical to T_C of ∼460 K from the fitting results.

The unique second-order transition of λ-Ti_3O_5 was further investigated from the broadening of diffraction peaks. Figure 4 shows the temperature-dependent full width at half maximum (FWHM) of the out-of-plane λ-Ti_3O_5 600 reflection along the 2θ ($\Delta 2\theta_{600}$), ω ($\Delta\omega_{600}$), and χ ($\Delta\chi_{600}$) directions. The 2θ, ω, and χ directions corresponded to the λ-Ti_3O_5 [100], [001], and [010] directions, respectively (inset of Fig. 4). Thus, the variation in the FWHM reflects structural changes along the crystallographic directions, which was first accessible using single-crystalline specimens. Interestingly, $\Delta\omega_{600}$ was modulated in temperatures in sharp contrast to the almost constant values of $\Delta 2\theta_{600}$ and $\Delta\chi_{600}$. As shown in Fig. 4, $\Delta\omega_{600}$ remained unchanged in region I, began wider at 350 K, took a maximum value at 460 K, and decreased in

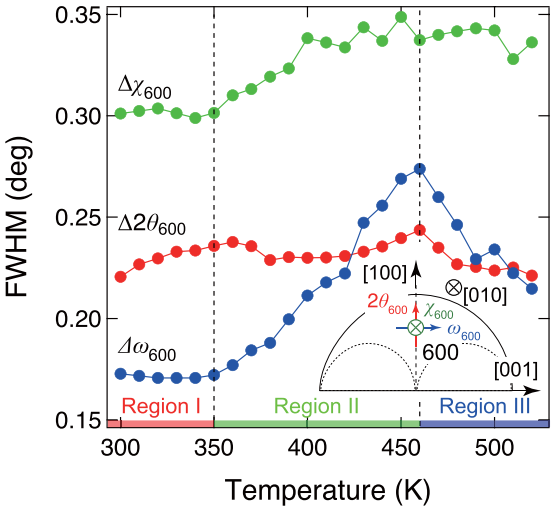

FIG. 4. Temperature-dependent full width at half maximum (FWHM) of λ-Ti_3O_5 600 reflections along the 2θ ($\Delta 2\theta_{600}$), ω ($\Delta\omega_{600}$), and χ ($\Delta\chi_{600}$) directions. The inset shows a relationship between the λ-Ti_3O_5 crystallographic directions and the XRD configuration used in this paper.

region III. Note that the $\Delta\omega_{600}$ behavior is responsible for the intensity variation in the λ-Ti_3O_5 600 reflections, as shown in Fig. 2(a). These results indicate the existence of two characteristic temperatures of 350 and 460 K. The former temperature corresponds to that of the resistivity kink [Fig. 1(a)] and the sign reversal of the thermal lattice expansion [Fig. 2(b)]. The latter temperature was identical to T_C determined from the β angle [Fig. 3(b)]. The excellent agreement of the characteristic temperatures between the electrical and structural properties further supports that the modulation in $\Delta\omega_{600}$ closely correlates with the phase transition in λ-Ti_3O_5.

We schematically summarized the structural and electronic phases of λ-Ti_3O_5 in Fig. 5. The resistivity of the monoclinic λ phase followed the Mott VRH model with three-dimensional conduction at low temperatures. Accordingly, the insulating λ phase was stable in region I. The resistivity curve showed a kink structure at 350 K, which was a signature of the MIT. The crystal symmetry remained intact across 350 K, thereby representing the conductive λ phase in region II (350 K $\leqslant T \leqslant$ 460 K). The resistivity in region II followed the Mott VRH model with three-dimensional conduction, although the characteristic parameters differed from those in region I. The gradual β-angle deformation occurred in temperature, and the orthorhombic α phase appeared at 460 K (regions II and III

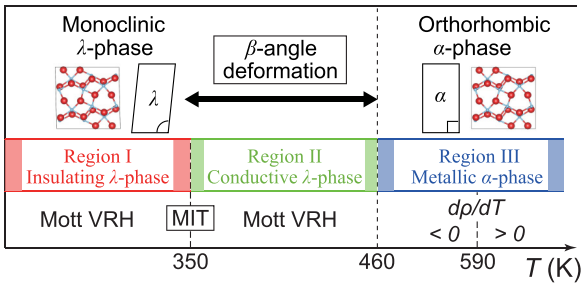

FIG. 5. Structural and electronic phase diagrams of λ-Ti_3O_5.

border). Thus, the metallic α phase was stable in region III, and the sign of $d\rho/dT$ became positive above ∼590 K. We note that metallic conductivity in the α phase is demonstrated in this paper, as predicted by the first-principles calculations based on density functional theory (DFT) [25,38].

IV. DISCUSSION

Firstly, we discuss a plausible model for the structural phase transition. Compared with the crystal structures of λ-Ti_3O_5 and α-Ti_3O_5, Ti and O atomic positions are almost identical, despite their individual polymorphs (see Figs. 5 and S1 in the Supplemental Material [39]). The β angle, which is the dominant distinction in the polymorphs, gradually became orthogonal across the second-order structural phase transition. The β-angle deformation was caused by shifting the Ti and O atomic positions with thermal vibration, which was observed as a fluctuation in the crystal lattice from the XRD analysis (Fig. 4). Since we set the ω axis to coincide with the λ-Ti_3O_5 [001] direction (inset of Fig. 4), the broad $\Delta\omega_{600}$ suggested the dominant vibration of the atoms along the λ-Ti_3O_5 [001] direction. Nearly constant $\Delta 2\theta_{600}$ and $\Delta\chi_{600}$ in the whole temperature also supported the dominant structural fluctuation along the λ-Ti_3O_5 [001] direction. The beginning of broad $\Delta\omega_{600}$ and the sign reversal of the thermal lattice expansion at ∼350 K suggested that the structural phase transition was suppressed at the insulating λ-Ti_3O_5.

A maximal $\Delta\omega_{600}$ suggested that fluctuation was most intense at 460 K, corresponding to T_C determined from the β angle [Fig. 3(b)]. A monotonic increase in $\Delta\omega_{600}$ with a broad temperature range of ∼100 K suggested the gradual structural change. It is worth mentioning that a gradual lattice deformation is also observed for Ti_2O_3 in a broad temperature range of ∼150 K accompanying a semiconductor-semimetal transition [40–43]. Here, $\Delta\omega_{600}$ decreased in region III with increasing temperature, implying that slight fluctuation might persist in the α phase. These results suggest that the observed second-order structural phase transition between the λ to α phases originates from lattice fluctuation along the λ-Ti_3O_5 [001] direction owing to similar atomic positions of the two phases. We confirmed the reversibility of the structural phase transition by comparing the XRD patterns before and after heating, whereas 180° rotational domains slightly appeared due to the lowering of crystal symmetry in the cooling process (Fig. 8, see Appendix C).

Next, we discuss the electronic properties of λ-Ti_3O_5. As shown in Fig. 1(a), the λ-Ti_3O_5 film showed an insulating behavior ($d\rho/dT < 0$) in region I. The film resistivity was two orders of magnitude lower than that of β-Ti_3O_5 at 300 K [27], which was consistent with the prediction of the first-principles calculation [38]. Meanwhile, compared with the λ-Ti_3O_5 nanoparticles [11] and the λ-Ti_3O_5/$MgTi_2O_5$ multilayer [34], the insulating λ-Ti_3O_5 showed higher resistivity by an order of magnitude. The lower resistivity of the λ-Ti_3O_5 nanoparticles and the λ-Ti_3O_5/$MgTi_2O_5$ multilayer may be due to difficulty in quantitative electrical measurements of nanoparticle specimens and unintentional Mg doping from a $MgTi_2O_5$ layer to λ-Ti_3O_5 films [26], respectively.

The insulating ground states of λ-Ti_3O_5 were confirmed using hard x-ray photoemission spectroscopy (HAXPES) taken at 300 K (Fig. 9, see Appendix D). For the valence-band

spectrum shown in Fig. 9(b), a clear Ti $3d$ density of states appeared ∼1 eV, and a finite energy gap opened at E_F. The observation of a small energy gap was consistent with the insulating ρ-T behavior in region I [Fig. 1(a)]. It should be noted that the Ti $2p_{3/2}$ core level shown in Fig. 9(a) consisted of a dominant Ti^{3+} component and a shoulder Ti^{4+} one with a peak-height ratio of ∼2:1. The consistency with the nominal $Ti^{3.33+}$ in Ti_3O_5 guarantees that the present HAXPES measurements reveal intrinsic electronic structures of λ-Ti_3O_5 films.

To further discuss the electrical properties of the λ-Ti_3O_5 film, we analyzed ρ_0 and T_0 in Eq. (1). In the Mott VRH model, they are expressed in the following equations [33,34]:

$$\rho_0 = A\left[\frac{N(E_F)}{\alpha k_B T}\right]^{1/2}, \tag{2}$$

$$T_0 = \frac{24\alpha^3}{\pi k_B N(E_F)}, \tag{3}$$

where $N(E_F)$ is the number of localized states around the Fermi level (E_F), α is a localization parameter, k_B is the Boltzmann constant, and A is a phonon-derived constant. The equations represent that ρ_0 and T_0 are functions of α and $N(E_F)$. We calculated the $N(E_F)$ ratio between regions I and II from ρ_0 and T_0 values, as shown in Figs. 1(b) and 1(c). Here, $N(E_F)$ in region II was $\sim 3 \times 10^3$ times larger than that in region I, which was reasonable for the higher conductive nature of λ-Ti_3O_5 films in region II. We thus concluded that the electronic ground state of λ-Ti_3O_5 was an insulator inconsistent with a prediction from the first-principles calculation [11].

The inconsistency in the electronic ground states of λ-Ti_3O_5 between the experiment and calculation would originate from some charge/orbital order at low temperatures, which is observed in various transition-metal oxides [44–46]. Although the existence of the charge/orbital order is not confirmed at present, the possible charge order of λ-Ti_3O_5 was deduced from structural similarity to β-Ti_3O_5 (see Fig. S2 in the Supplemental Material [39]). In β-Ti_3O_5 having three inequivalent Ti sites, a charge order occurred with the valence of $+3(d^1)$, $+3.33(d^{0.67})$, and $+3.67(d^{0.33})$ at Ti_1, Ti_2, and Ti_3, respectively, [1,10] with an assistance of electron correlation. Consequently, the Ti_1-Ti_1 distance (2.61 Å) became shortest among other Ti-Ti pairs (>2.8 Å) owing to formation of Ti_1-Ti_1 direct bonding via t_{2g} orbitals. Because the dominant structural difference between β-Ti_3O_5 and λ-Ti_3O_5 is the Ti_3 atomic position, the Ti_1-Ti_1 distance is shortest in λ-Ti_3O_5 (= 2.73 Å) [11], suggesting the largest electron occupancy at the Ti_1 site for λ-Ti_3O_5 as well. This implies occurrence of charge order in λ-Ti_3O_5 like that in β-Ti_3O_5.

Meanwhile, the possible orbital order was deduced from similarity of the MIT behavior to $MgTi_2O_4$ [47–49] (see

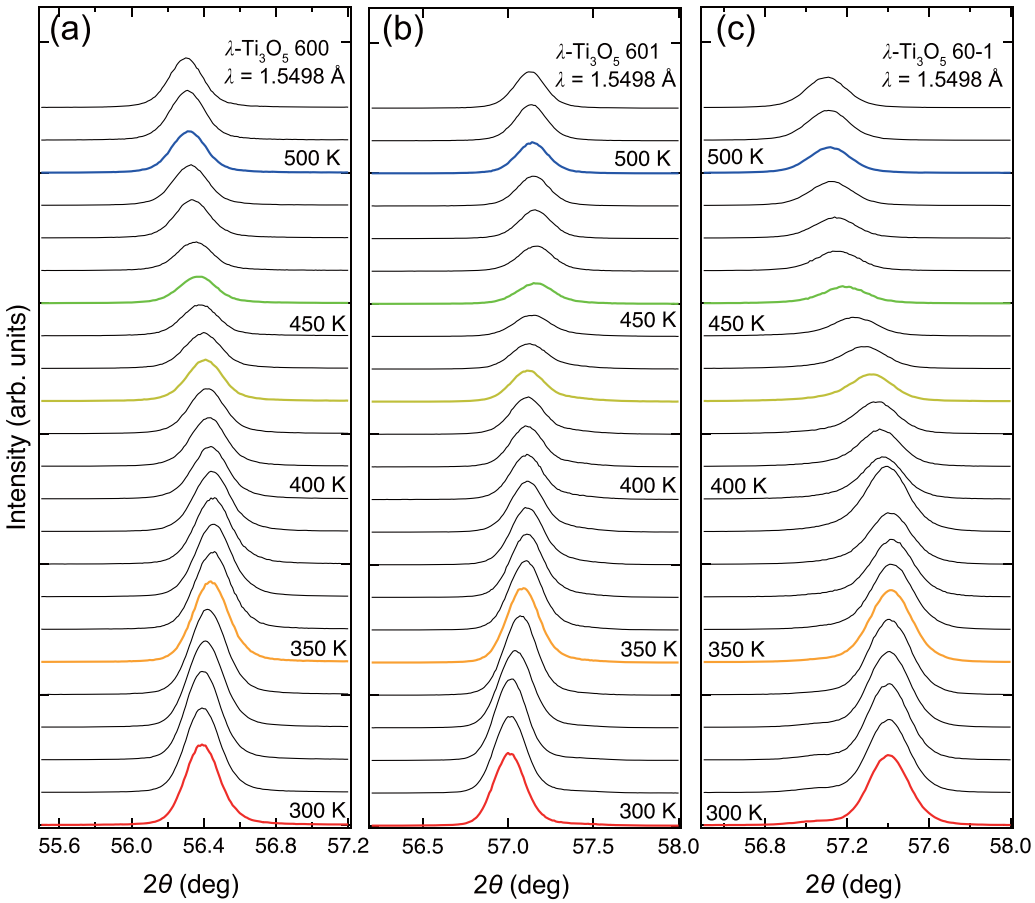

FIG. 6. Temperature-dependent synchrotron x-ray diffraction (XRD) patterns of (a) λ-Ti_3O_5 600, (b) λ-Ti_3O_5 601, and (c) λ-Ti_3O_5 60–1 reflections. The colors correspond to those in Figs. 2(a) and 3(a).

Fig. S3 in the Supplemental Material [39]). The temperature-dependent resistivity curves across the MIT were similar between the λ-Ti_3O_5 Ti_3O_5 films and $MgTi_2O_4$ although T_{MIT} differed by ∼100 K [47]. $MgTi_2O_4$ shows a one-dimensional helical dimer pattern in an insulating phase [48], and the dimer structure originates from a d_{yz}/d_{zx} orbital order [49]. These results imply that a similar orbital order occurs in the insulating λ-Ti_3O_5. To verify the possible charge/orbital order responsible for the insulating λ-Ti_3O_5, further structural and electronic investigations are required. Detailed structural analysis across the electronic phase transition would provide crucial information about the charge/orbital order by observing superstructures.

V. SUMMARY

We investigated the structural and electrical properties of single-crystalline λ-Ti_3O_5 films across the temperature-induced phase transition. The synchrotron XRD measurements revealed the second-order structural phase transition between monoclinic λ-Ti_3O_5 and orthorhombic α-λ-Ti_3O_5 with the gradual β-angle deformation. The structural phase transition was characterized by fluctuation in crystal lattice along the λ-Ti_3O_5 [001] direction. The ρ-T measurements revealed the resistivity kink at 350 K attributed to the MIT. Based on the synchrotron XRD and ρ-T results, we draw the electronic and structural phase diagram of Ti_3O_5 separated into three temperature regions. The insulating λ phase was stabilized at $T \leqslant 350$ K. The conductive λ phase appeared at $350\ \text{K} \leqslant T \leqslant 460$ K via the MIT. The metallic orthorhombic α phase was stabilized at $T \geqslant 460$ K across the gradual second-order structural phase transition from the monoclinic λ phase. In this paper, we demonstrated the complex electronic and structural phase transitions in Ti_3O_5 polymorphs. Our findings provide a significant step for controlling phase transitions in Ti_3O_5 polymorphs using external stimuli, which is crucial for optoelectronic and heat-storage applications of Ti_3O_5.

ACKNOWLEDGMENTS

We thank R. Kumashiro and K. Saitoh in the common equipment room of WPI in Tohoku University for the film-thickness measurements and Raman spectroscopy. The scanning TEM (STEM) measurements were performed under the approval of MEXT Nanotechnology Platform Japan (Grant No. A-21-TU-0001). We thank S. Ito, K. Takenaka, and Y. Hayasaka for the STEM measurements. This paper was partly supported by MEXT Elements Strategy Initiative to Form Core Research Center (Grant No. JPMXP0112101001), a Grant-in-Aid for Scientific Research (Grants No. 22H01947 and No. 22H01948) from the Japan Society for the Promotion of Science Foundation, CREST (Grant No. JPMJCR18T1) from the Japan Science and Technology Agency, Hattori Hokokai Foundation, Kato Foundation for Promotion of Science, and Murata Science Foundation. The synchrotron XRD measurements were done under the approval of the Program Advisory Committee (Proposal No. 2018S2-004). The hard x-ray photoemission measurements at SPring-8 were done under the approval of the Japan Synchrotron Radiation Research Institute (Proposal No. 2022B1574).

APPENDIX A: TEMPERATURE-DEPENDENT SYNCHROTRON XRD PATTERNS

Figure 6 shows synchrotron XRD patterns of the λ-Ti_3O_5 films taken in a heating procedure ranging from 300 to 520 K. The typical XRD patterns of the λ-Ti_3O_5 600 and 60 ± 1 reflections [Figs. 2(a) and 3(a), respectively] were selected from Fig. 6.

APPENDIX B: HIGH-ANGLE ANNULAR DARK FIELD-SCANNING TEM IMAGES OF λ-Ti_3O_5/$LaAlO_3$ INTERFACE

Scanning TEM (STEM) measurements using Titan (FEI Company) were conducted at 300 K to observe crystal structures of the films on an atomic scale. An applied voltage of 300 kV accelerated electrons to obtain high-resolution high-angle annular dark field (HAADF)-STEM images. We performed HAADF-STEM measurements on the as-grown film and a film that once underwent a temperature-induced structural phase transition. We refer to the latter as a *heated film* hereafter. Both films were thinned down to electron transparency using the focused ion beam etching technique. STEM images of λ-Ti_3O_5 crystal structures were simulated using Dr. Probe software [50] with parameters identical to those in experiments.

Figure 7 shows the HAADF-STEM images of the λ-Ti_3O_5 films taken at 300 K along the λ-Ti_3O_5 [001] and [010] directions. Bright zigzag chains were observed in the as-grown

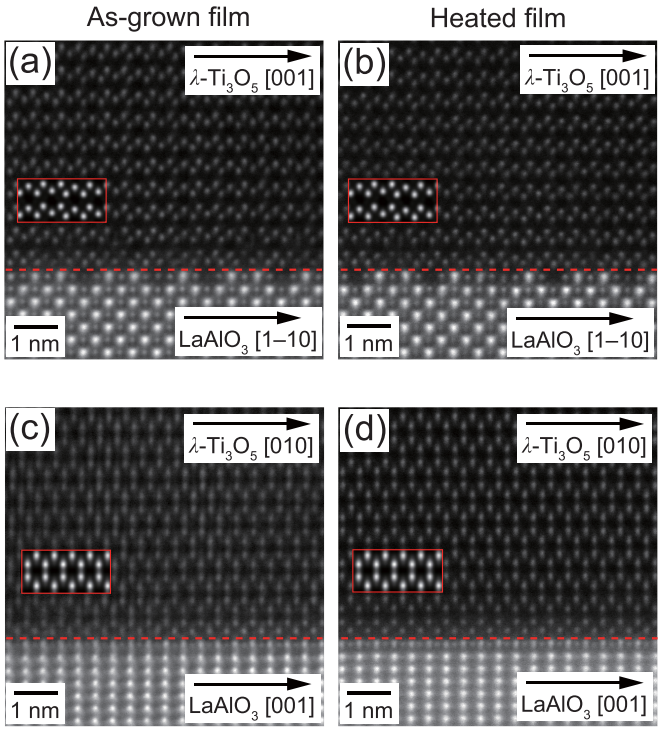

FIG. 7. High-angle annular dark field (HAADF) scanning transmission electron microscopy (STEM) images of (a) and (c) as-grown and (b) and (d) heated λ-Ti_3O_5 films taken along the λ-Ti_3O_5 [001] and [010] directions. The dashed lines indicate the λ-Ti_3O_5/$LaAlO_3$ interface. The STEM simulations of λ-Ti_3O_5 are indicated by red squares.

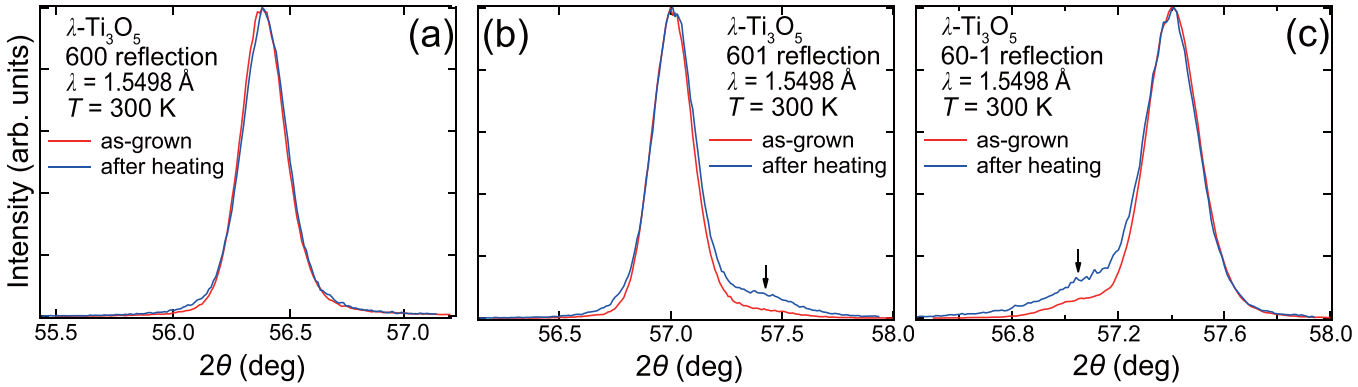

FIG. 8. Synchrotron x-ray diffraction (XRD) patterns of (a) λ-Ti_3O_5 600, (b) λ-Ti_3O_5 601, and (c) λ-Ti_3O_5 60–1 reflections for as-grown (red) and heated (blue) films taken at 300 K. The arrows in (b) and (c) indicate shoulder structures derived from 180° rotational domains.

[Fig. 7(a)] and heated [Fig. 7(b)] films along the λ-Ti_3O_5 [001] direction, which was expected from the configuration of the Ti atoms in λ-Ti_3O_5 (see Fig. S1 in the Supplemental Material [39]). The honeycomb structures of bright spots were aligned along the λ-Ti_3O_5 [010] direction for both as-grown [Fig. 7(c)] and heated [Fig. 7(d)] films. To confirm the λ-phase crystal structure, we performed STEM simulations to λ-Ti_3O_5, and an obtained image was overlayed in Fig. 7. The simulated images reproduced well the experimental ones, indicating that both the as-grown and heated films were λ-Ti_3O_5. The λ phase of the heated film was also confirmed by synchrotron XRD measurements (see Fig. 8). These results demonstrate that temperature induces the structural phase transition and that neither degradation nor oxidation in the heating procedure affects the structural and electronic properties.

APPENDIX C: SYNCHROTRON XRD PATTERNS OF AS-GROWN AND HEATED λ-Ti_3O_5 FILMS AT 300 K

Figure 8 shows synchrotron XRD patterns of the λ-Ti_3O_5 600 and 60 ± 1 reflections for the as-grown and heated films taken at 300 K. The reflections were almost identical in both films, suggesting the identical crystal structure between the as-grown and heated films at 300 K. A slight increase in the shoulder structures was detected for the λ-Ti_3O_5 60 ± 1 reflections in the heated film due to the 180° rotational domains. In a cooling procedure, the films underwent the structural phase transition from the orthorhombic α phase to the monoclinic λ phase. Accordingly, the 180° rotational domains would be partially formed in the heated film, which was responsible for the shoulder structures.

APPENDIX D: HAXPES SPECTRA OF λ-Ti_3O_5 FILMS

HAXPES was conducted at BL09XU of SPring-8 at 300 K. To prevent surface oxidation in air, the λ-Ti_3O_5 film was capped with 10-nm-thick amorphous Al_2O_3 layers. Figure 9(a) shows the Ti 2*p* core-level spectrum of the λ-Ti_3O_5 film. The Ti $2p_{3/2}$ core level consisted of a dominant Ti^{3+} component at ∼458 eV and a shoulder Ti^{4+} component at ∼460 eV with their peak-height ratio of ∼2:1, which was consistent in the nominal valence of $Ti^{3.33+}$ in Ti_3O_5. The result suggests that the HAXPES measurements can reveal intrinsic electronic structures of λ-Ti_3O_5 films [51]. We thus recorded the valence band spectrum of the film [Fig. 9(b)]. The spectrum was composed of O 2*p* structures from ∼15 to 4 eV and Ti 3*d* ones near the Fermi level (E_F). From the magnification of Ti 3*d* states [inset of Fig. 9(b)], a finite energy gap of ∼0.2 eV was clearly observed at E_F, which agreed with the insulating ρ-*T* behavior of λ-Ti_3O_5 films at 300 K [Fig. 1(a)].

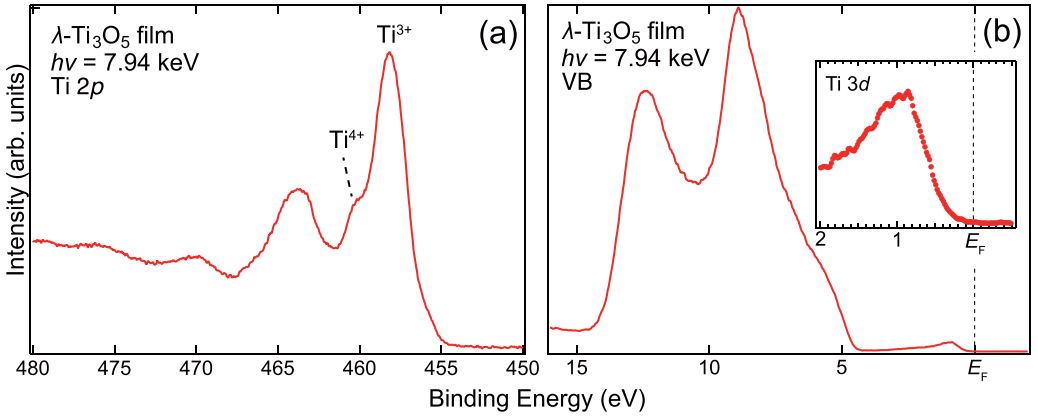

FIG. 9. (a) Ti 2*p* core-level and (b) valence-band spectra of λ-Ti_3O_5 films taken at 300 K. The inset in (b) shows a magnification of Ti 3*d* states near the Fermi level (E_F).

[1] S. Åsbrink, L. Gerward, and J. S. Olsen, A high-pressure study of Ti_3O_5 by x-ray diffraction and synchrotron radiation. 1. Pressures up to 38.6 GPa, J. Appl. Cryst. **22**, 119 (1989).

[2] R. Roy, V. G. Hill, and E. F. Osborn, Polymorphism of Ga_2O_3 and the system $Ga_2O_3-H_2O$, J. Am. Chem. Soc. **74**, 719 (1952).

[3] M. Bosi, P. Mazzolini, L. Seravalli, and R. Fornari, Ga_2O_3 polymorphs: Tailoring the epitaxial growth conditions, J. Mater. Chem. C **8**, 10975 (2020).

[4] D. Aulakh, J. R. Varghese, and M. Wriedt, The importance of polymorphism in metal-organic framework studies, Inorg. Chem. **54**, 8679 (2015).

[5] A. J. Cruz-Cabeza and J. Bernstein, Conformational polymorphism, Chem. Rev. **114**, 2170 (2014).

[6] P. T. B. Shaffer, A review of the structure of silicon carbide, Acta Cryst. B **25**, 477 (1969).

[7] M. Wuttig and N. Yamada, Phase-change materials for rewriteable data storage, Nat. Mater. **6**, 824 (2007).

[8] A. Fujishima, X. Zhang, and D. A. Tryk, TiO_2 photocatalysis and related surface phenomena, Surf. Sci. Rep. **63**, 515 (2008).

[9] S. -H. Hong and S. Åsbrink, The structure of γ-Ti_3O_5 at 297 K, Acta Cryst. B **38**, 2570 (1982).

[10] S. Åsbrink and A. Magnéli, Crystal structure studies on trititanium pentoxide, Ti_3O_5, Acta Cryst. **12**, 575 (1959).

[11] S. Ohkoshi, Y. Tsunobuchi, T. Matsuda, K. Hashimoto, A. Namai, F. Hakoe, and H. Tokoro, Synthesis of a metal oxide with a room-temperature photoreversible phase transition, Nat. Chem. **2**, 539 (2010).

[12] M. Onoda, Phase transitions of Ti_3O_5, J. Solid State Chem. **136**, 67 (1998).

[13] K. Tanaka, T. Nasu, Y. Miyamoto, N. Ozaki, S. Tanaka, T. Nagata, F. Hakoe, M. Yoshikiyo, K. Nakagawa, Y. Umeta *et al.*, Structural phase transition between γ-Ti_3O_5 and δ-Ti_3O_5 by breaking of a one-dimensionally conducting pathway, Cryst. Growth Des. **15**, 653 (2015).

[14] P. Zhao, G. Li, W. Li, P. Cheng, Z. Pang, X. Xiong, X. Zou, Q. Xu, and X. Lu, Progress in Ti_3O_5: Synthesis, properties and applications, Trans. Nonferrous Met. Soc. China **31**, 3310 (2021).

[15] A. Ould-Hamouda, H. Tokoro, S.-I. Ohkoshi, and E. Freysz, Single-shot time resolved study of the photo-reversible phase transition induced in flakes of Ti_3O_5 nanoparticles at room temperature, Chem. Phys. Lett. **608**, 106 (2014).

[16] R. Liu and J.-X. Shang, First-principles study of thermal properties and phase transition between β-Ti_3O_5 and λ-Ti_3O_5, Modeling Simul. Mater. Sci. Eng. **20**, 035020 (2012).

[17] H. Tokoro, M. Yoshikiyo, K. Imoto, A. Namai, T. Nasu, K. Nakagawa, N. Ozaki, F. Hakoe, K. Tanaka, K. Chiba *et al.*, External stimulation-controllable heat-storage ceramics, Nat. Commun. **6**, 7037 (2015).

[18] S. Ohkoshi, H. Tokoro, K. Nakagawa, M. Yoshikiyo, F. Jia, and A. Namai, Low-pressure-responsive heat-storage ceramics for automobiles, Sci. Rep. **9**, 13203 (2019).

[19] C. Mariette, M. Lorenc, H. Cailleau, E. Collet, L. Guérin, A. Volte, E. Trzop, R. Bertoni, X. Dong, B. Lépine *et al.*, Strain wave pathway to semiconductor-to-metal transition revealed by time-resolved x-ray powder diffraction, Nat. Commun. **12**, 1239 (2021).

[20] A. Asahara, H. Watanabe, H. Tokoro, S.-i. Ohkoshi, and T. Suemoto, Ultrafast dynamics of photoinduced semiconductor-to-metal transition in the optical switching nano-oxide Ti_3O_5, Phys. Rev. B **90**, 014303 (2014).

[21] K. R. Tasca, V. Esposito, G. Lantz, P. Beaud, M. Kubli, M. Savoini, C. Giles, and S. L. Johnson, Time-resolved x-ray powder diffraction study of photoinduced phase transitions in Ti_3O_5 nanoparticles, ChemPhysChem **18**, 1385 (2017).

[22] R. Makiura, Y. Takabayashi, A. N. Fitch, H. Tokoro, S. Ohkoshi, and K. Prassides, Nanoscale effects on the stability of the λ-Ti_3O_5 polymorph, Chem. Asian J. **6**, 1886 (2011).

[23] T. Saiki, T. Yoshida, K. Akimoto, D. Indo, M. Arizono, T. Okuda, and T. Katsufuji, Selection rule for the photoinduced phase transition dominated by anisotropy of strain in Ti_3O_5, Phys. Rev. B **105**, 075134 (2022).

[24] Y. Nakamura, Y. Sakai, M. Azuma, and S. Ohkoshi, Long-term heat-storage ceramics absorbing thermal energy from hot water, Sci. Adv. **6**, eaaz5264 (2020).

[25] D. Olguín, E. Vallejo, and A. Rubio-Ponce, *Ab initio* study of the low-pressure phases of Ti_3O_5, Physica Status Solidi B **252**, 659 (2015).

[26] M. Wang, W. Huang, Z. Shen, J. Gao, Y. Shi, T. Lu, and Q. Shi, Phase evolution and formation of λ phase in Ti_3O_5 induced by magnesium doping, J. Alloy Compd. **774**, 1189 (2019).

[27] R. Takahama, T. Ishii, D. Indo, M. Arizono, C. Terakura, Y. Tokura, N. Takeshita, M. Noda, H. Kuwahara, T. Saiki *et al.*, Structural, magnetic, transport, and thermoelectric properties of the pseudobrookite $AlTi_2O_5-Ti_3O_5$ system, Phys. Rev. Mater. **4**, 074401 (2020).

[28] Z. Shen, Q. Shi, W. Huang, B. Huang, M. Wang, J. Gao, Y. Shi, and T. Lu, Stabilization of microcrystal λ-Ti_3O_5 at room temperature by aluminum-ion doping, Appl. Phys. Lett. **111**, 191902 (2017).

[29] K. Yoshimatsu and H. Kumigashira, Direct synthesis of metastable λ-phase Ti_3O_5 films on $LaAlO_3$ (110) substrates at high temperatures, Cryst. Growth Des. **22**, 703 (2022).

[30] H. Kurokawa, K. Yoshimatsu, O. Sakata, and A. Ohtomo, Effects of phase fraction on superconductivity of low-valence eutectic titanate films, J. Appl. Phys. **122**, 055302 (2017).

[31] K. Yoshimatsu, O. Sakata, and A. Ohtomo, Superconductivity in Ti_4O_7 and γ-Ti_3O_5 films, Sci. Rep. **7**, 12544 (2017).

[32] H. Chen, Y. Hirose, K. Nakagawa, K. Imoto, S. Ohkoshi, and T. Hasegawa, Non-metallic electrical transport properties of a metastable λ-Ti_3O_5 thin film epitaxially stabilized on a pseudobrookite seed layer, Appl. Phys. Lett. **116**, 201904 (2020).

[33] N. F. Mott, Conduction in glasses containing transition metal ions, J. Non-Cryst. Solids **1**, 1 (1968).

[34] N. Mott and E. Davis, *Electronic Processes in Non-Crystalline Materials*, 2nd ed. (Clarendon Press, Oxford, 1979), pp. 32–37.

[35] K. Momma and F. Izumi, VESTA 3 for three-dimensional visualization of crystal, volumetric and morphology data, J. Appl. Cryst. **44**, 1272 (2011).

[36] R. A. Cowley, Structural phase transitions I. Landau theory, Adv. in Phys. **29**, 1 (1980).

[37] A. D. Bruce, Structural phase transitions. II. Static critical behaviour, Adv. in Phys. **29**, 111 (1980).

[38] X.-K. Fu, B. Yang, W.-Q. Chen, Z.-S. Jiang, Z.-B. Li, H.-L. Yan, X. Zhao, and L. Zuo, Evidence for bandwidth-control

metal-insulator transition in Ti_3O_5, Compt. Mater. Sci. **173**, 109435 (2020).

[39] See Supplemental Material at http://link.aps.org/supplemental/10.1103/PhysRevMaterials.8.035002 for the crystal structures of λ-Ti_3O_5 and α-Ti_3O_5 and the possible charge and orbital order in λ-Ti_3O_5.

[40] K. Yoshimatsu, H. Kurokawa, K. Horiba, H. Kumigashira, and A. Ohtomo, Large anisotropy in conductivity of Ti_2O_3 films, APL Mater. **6**, 101101 (2018).

[41] K. Yoshimatsu, N. Hasegawa, Y. Nambu, Y. Ishii, Y. Wakabayashi, and H. Kumigashira, Metallic ground states of undoped Ti_2O_3 films induced by elongated *c*-axis lattice constant, Sci. Rep. **10**, 22109 (2020).

[42] K. Yoshimatsu, S. Miyazaki, N. Hasegawa, and H. Kumigashira, Evidence of lattice deformation induced metal-insulator transition in Ti_2O_3, Phys. Rev. B **106**, L081110 (2022).

[43] J. M. Honig and T. B. Reed, Electrical properties of Ti_2O_3 single crystals, Phys. Rev. **174**, 1020 (1968).

[44] Y. Tomioka, A. Asamitsu, Y. Moritomo, H. Kuwahara, and Y. Tokura, Collapse of a charge-ordered state under a magnetic field in $Pr_{1/2}Sr_{1/2}MnO_3$, Phys. Rev. Lett. **74**, 5108 (1995).

[45] J. A. Alonso, J. L. García-Muñoz, M. T. Fernández-Díaz, M. A. G. Aranda, M. J. Martínez-Lope, and M. T. Casais, Charge disproportionation in $RNiO_3$ perovskites: Simultaneous metal-insulator and structural transition in $YNiO_3$, Phys. Rev. Lett. **82**, 3871 (1999).

[46] J. M. Tranquada, B. J. Sternlieb, J. D. Axe, Y. Nakamura, and S. Uchida, Evidence for stripe correlations of spins and holes in copper oxide superconductors, Nature (London) **375**, 561 (1995).

[47] M. Isobe and Y. Ueda, Observation of phase transition from metal to spin-singlet insulator in $MgTi_2O_4$ with $S = \frac{1}{2}$ pyrochlore lattice, J. Phys. Soc. Jpn. **71**, 1848 (2002).

[48] M. Schmidt, W. Ratcliff, II, P. G. Radaelli, K. Refson, N. M. Harrison, and S. W. Cheong, Spin singlet formation in $MgTi_2O_4$: Evidence of a helical dimerization pattern, Phys. Rev. Lett. **92**, 056402 (2004).

[49] D. I. Khomskii and T. Mizokawa, Orbitally induced Peierls state in spinels, Phys. Rev. Lett. **94**, 156402 (2005).

[50] J. Barthel, Dr. Probe: A software for high-resolution STEM image simulation, Ultramicroscopy **193**, 1 (2018).

[51] K. Kobayashi, M. Taguchi, M. Kobata, K. Tanaka, H. Tokoro, H. Daimon, T. Okane, H. Yamagami, E. Ikenaga, and S.-i. Ohkoshi, Electronic structure and correlation in β-Ti_3O_5 and λ-Ti_3O_5 studied by hard x-ray photoelectron spectroscopy, Phys. Rev. B **95**, 085133 (2017).